RESEARCH ARTICLE

Key Points:
- Backscattering efficiency of solar wind protons from lunar surface: ~0.01%–1%
- Proton backscattering efficiency depends exponentially on impact speed
- Backscattered protons have peak exit speed at ~80% of impact speed

Correspondence to:
C. Lue,
charles.lue@irf.se

Chandrayaan-1 observations of backscattered solar wind protons from the lunar regolith: Dependence on the solar wind speed

Charles Lue[1,2], Yoshifumi Futaana[1], Stas Barabash[1], Martin Wieser[1], Anil Bhardwaj[3], and Peter Wurz[4]

[1]Swedish Institute of Space Physics, Kiruna, Sweden, [2]Department of Physics, Umeå University, Umeå, Sweden, [3]Space Physics Laboratory, Vikram Sarabhai Space Center, Trivandrum, India, [4]Physikalisches Institut, University of Bern, Bern, Switzerland

Abstract We study the backscattering of solar wind protons from the lunar regolith using the Solar Wind Monitor of the Sub-keV Atom Reflecting Analyzer on Chandrayaan-1. Our study focuses on the component of the backscattered particles that leaves the regolith with a positive charge. We find that the fraction of the incident solar wind protons that backscatter as protons, i.e., the proton-backscattering efficiency, has an exponential dependence on the solar wind speed that varies from ~0.01% to ~1% for solar wind speeds of 250 km/s to 550 km/s. We also study the speed distribution of the backscattered protons in the fast (~550 km/s) solar wind case and find both a peak speed at ~80% of the solar wind speed and a spread of ~85 km/s. The observed flux variations and speed distribution of the backscattered protons can be explained by a speed-dependent charge state of the backscattered particles.

1. Introduction

When solar wind protons impact the lunar regolith, a significant fraction is backscattered into space. This phenomenon was first observed for backscattered protons (H^{+}) [*Saito et al.*, 2008], and it was subsequently observed for hydrogen energetic neutral atoms (H ENA) [*McComas et al.*, 2009; *Wieser et al.*, 2009]. These observations have transformed our view of the interaction between the solar wind and the Moon and of plasma's interaction with atmosphereless bodies, in general [e.g., *Halekas et al.*, 2011]. Additionally, these observations provide a unique set of experimental results in the field of particle-surface interactions. Only limited laboratory knowledge exists regarding particle backscattering from insulators [e.g., *Winter*, 2000] and rough surfaces [e.g., *Bandurko et al.*, 1990].

Detailed studies of the backscattered H ENA have been performed recently. The reported backscattering efficiencies range between ~10% and ~20% [see *Vorburger et al.*, 2013, Table 2, and references therein]. In addition, the scattering function [*Schaufelberger et al.*, 2011] and the energy spectrum [*Futaana et al.*, 2012; *Rodríguez et al.*, 2012; *Allegrini et al.*, 2013] have been defined, and the spatial variability on the Moon [*Vorburger et al.*, 2013] has been investigated. Also, the temporal variability related to the solar wind conditions has been investigated: *Futaana et al.* [2012] reported variations in the energy spectrum in response to varying solar wind speed but found no other relation to the upstream conditions, whereas *Funsten et al.* [2013] reported a decrease in the backscattering efficiency with increasing solar wind speed.

Concerning the backscattered H^{+}, considerably fewer studies have been performed. *Saito et al.* [2008, 2010] reported an ~0.1%–1% H^{+} backscattering efficiency; a broad H^{+} scattering function, peaked roughly toward the zenith; and a broad H^{+} energy spread up to solar wind energies, which peaked at ~70% of the solar wind energy.

In the present study, we use Chandrayaan-1 ion data to make independent observations of the backscattered H^{+} and to investigate the dependence of the H^{+} backscattering efficiency on the solar wind speed.

2. Instrumentation and Data

The Solar Wind Monitor (SWIM) [*McCann et al.*, 2007] was an element of the Sub-keV Atom Reflecting Analyzer (SARA) [*Barabash et al.*, 2009] on the Chandrayaan-1 (CY-1) lunar orbiter. SWIM measured positive ions in the energy range from 100 eV to 3 keV divided into 16 energy channels and had a fan-like (~7° × 160°) field of view (FOV) divided into 16 angular channels (D0 to D15). The FOV was oriented perpendicularly to the
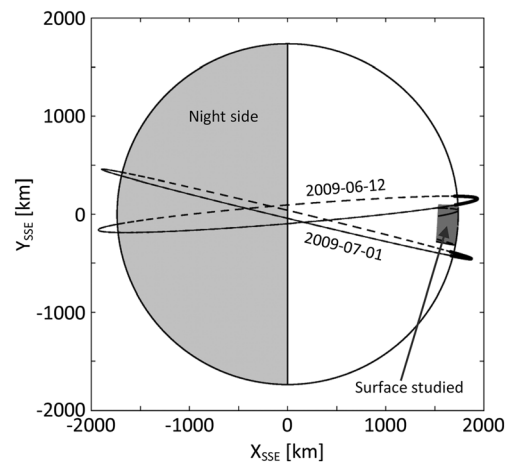
Figure 1. The orbit configuration and viewing conditions for the data used in the present study, shown in Selenocentric Solar Ecliptic (SSE) coordinates (i.e., from the origin at the Moon's center, the X_{SSE} axis points to the Sun, and Z_{SSE} is perpendicular to the ecliptic plane, pointing north). The first and last orbits of the study are plotted; the other orbits studied lie between these. We only use data collected within ±10 min (corresponding to ±28°) of the dayside equator crossing. In the two orbits shown, these times are indicated with thick lines. The observation footprints, i.e., the surface viewed by SWIM, direction D0 (27° off nadir), for these times are indicated by lines on the lunar surface. The corresponding surface coverage of the orbits in between is indicated by the dark grey area. The spacecraft orientation relative to the surface was flipped once during the study (while crossing the noon-midnight meridian), such that the SWIM footprint is westward of the orbit before and eastward of the orbit after the flip.

spacecraft velocity vector and spanned nearly from nadir to zenith [cf. *Futaana et al.*, 2010b, Figure 1]. At each time, one direction channel and one energy channel are active. A full sweep through the 16×16 energy-direction combinations was performed every 8 s.

For this study, we chose a time period when the Moon was upstream of the terrestrial bow shock and the CY-1 orbit was close to the noon-midnight meridian (see Figure 1). From each orbit, we used the 20 min of data closest to CY-1's dayside crossing of the lunar equator. This period corresponds to latitudes of ≲30° and longitudes of ≲20° from the subsolar point. These criteria select measurements near the subsolar point, where the incident solar wind flux on the lunar surface is the highest. Orbits in which the attitude of CY-1 deviated by >15° from the nominal nadir pointing or in which SWIM did not operate for the full 20 min around the equator crossing were not included. When these criteria were applied, 70 orbits were identified for inclusion in this study, and all of them were within the time period of 12 June to 1 July 2009. During this time, CY-1 had a circular polar orbit at an altitude of 200 km. We used data from the Wind spacecraft (located at 245–261 Earth radii upstream of the Earth) to obtain the corresponding solar wind plasma and interplanetary magnetic field (IMF) parameters; these data were time shifted (typically ~1 h) accounting for the instantaneous Wind-Moon distance and the solar wind velocity measured at Wind.

3. Observations

Figure 2 presents the SWIM observations collected during one equator passage on 29 June 2009. During this passage, the solar wind flux was $1.8 \times 10^8 \, \text{cm}^{-2} \, \text{s}^{-1}$, the velocity was 550 km/s, and the IMF strength was 4.1 nT. Three major ion populations can be identified, and (1) the first population is the solar wind (Figures 2a and 2c). Because of the finite acceptance angle as a function of the elevation and solar wind thermal spreading, the solar wind was observed over the interval 14:59–15:14, and its maximum was at 15:06. (2) The second population is the H^+ flux deflected from lunar magnetic anomalies (LMAs) (Figures 2b and 2c; ~15:13–15:19 UT). The characteristics of this population are recognizable from earlier studies [*Saito et al.*, 2010; *Lue et al.*, 2011]; specifically, its energy is near the solar wind energy, and it has a wider energy spread than the solar wind. This population comes from the LMA locations (Figure 2d). (3) The third population is classified as backscattered H^+ (Figures 2b and 2c; ~14:59–15:12 UT), which exhibits a broad spread in energy and direction and comes from surface directions that have no apparent correlation to LMAs (Figure 2d). Its energy is below the solar wind energy. These characteristics are consistent with the previous observations by *Saito et al.* [2008].
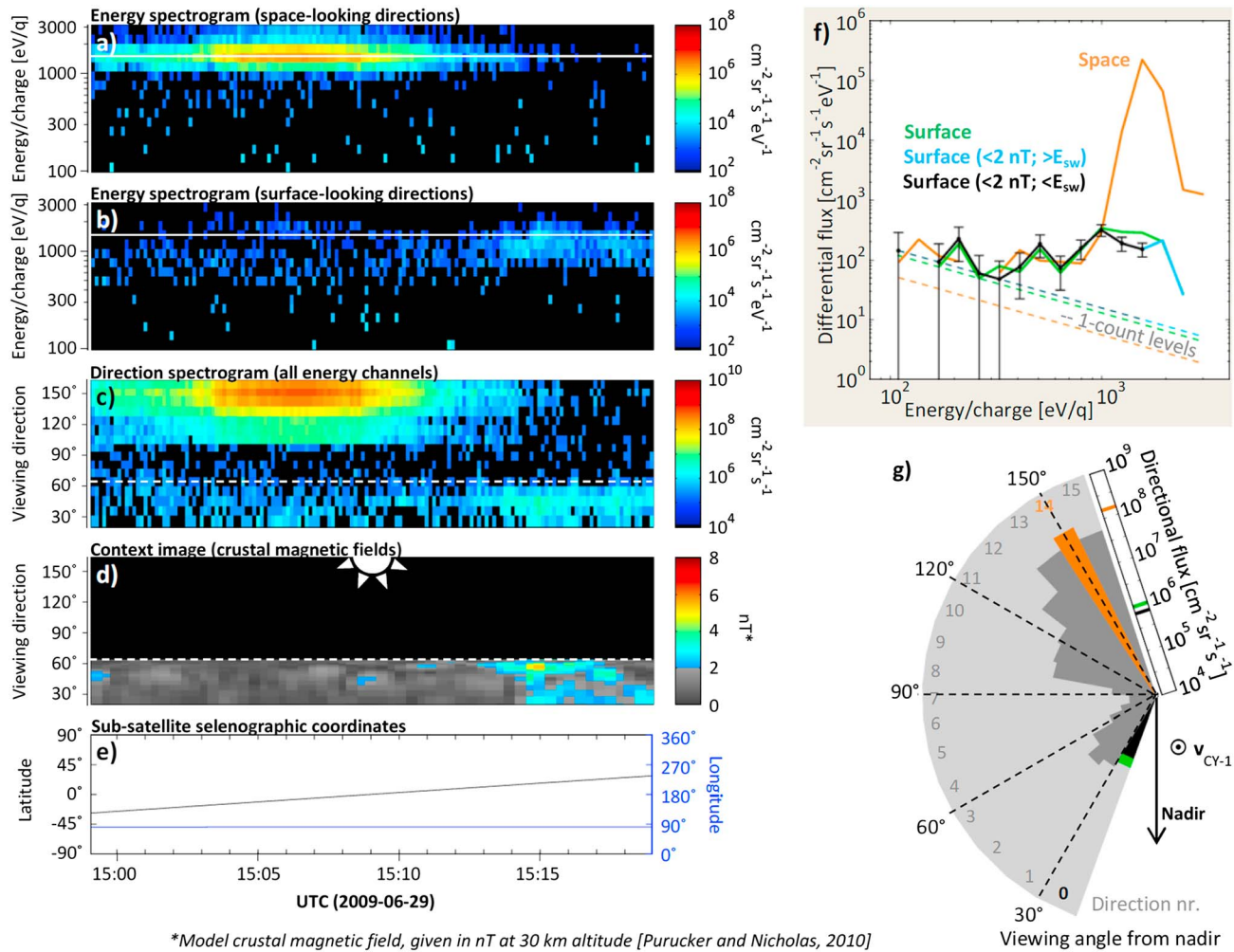
4. Analysis

For our further analysis of the backscattered H^+ population, we focus on the viewing direction closest to the nadir (D0) and on energies up to the solar wind peak. D0 is chosen because it is favorable for backscattered H^+ from the surface and unfavorable for deflected H^+ from LMAs [cf. *Saito et al.*, 2010, Figures 22 and 24]. To further reduce the counts attributable to deflected H^+ from LMAs, we exclude all of the data that were obtained when LMAs (with a threshold set to 2 nT at 30 km) were in the D0 FOV.

The energy spectrum of D0 before and after the exclusion of LMAs is shown in Figure 2f. The solar wind spectrum recorded for D14 is also shown for reference. The D0 energy spectrum is susceptible to instrument

Figure 2. SWIM observations, 14:59–15:19 UTC on 29 June 2009. (a and b) Energy spectrograms of the differential flux from D13 to D15 (space-looking directions) and D0–D2 (surface-looking directions). The solid lines indicate the solar wind energy (calculated for protons, using the mean solar wind speed given by Wind). (c) A direction spectrogram of the directional flux integrated over all energy channels. (d) A lunar magnetic anomaly's strength at 30 km in altitude [*Purucker and Nicholas*, 2010], as seen within the instrument's field of view. The dashed lines indicate the lunar limb. (e) Selenographic coordinates of the subsatellite point. (f) The averaged energy spectrum over the time interval for the D14 (space; orange) and D0 (surface; green) directions. The energy spectrum of the D0 direction after the exclusion of magnetic anomalies is shown in black (up to the solar wind energy) and cyan (above the solar wind energy). The black curve is shown with 1σ Poisson error bars. The dashed lines in Figure 2f correspond to one count during the period. (g) The averaged directional fluxes in the spacecraft coordinate system. The color coding in Figure 2g is the same as in Figure 2f.

crosstalk from the solar wind. The crosstalk results in a weak signal, which is at the level of a small fraction (10^{-4}) of the solar wind counts from the lower neighboring energy channel. However, because the crosstalk is strongest at the energy channel one step up from the solar wind energy, it does not significantly affect our results, which are based on energy channels up to the solar wind peak. There is also an instrument background, contributing on average with 1.6 counts per energy-direction bin per 20 min. This background's contribution is negligible in the case shown in Figure 2. In the general case, however, we need to account for this background. We address this issue in the following sections.

We integrate the signal over the energy and obtain the average directional fluxes (Figure 2g). The solar wind peak is at D14, and the peak at D2 is dominated by H^+ deflected from the LMAs. For D0, the slightly lower directional flux obtained after excluding the LMAs and limiting the energy range is also shown. To calculate the flux of backscattered H^+, we use this lower result from D0 and assume an isotropic (2π sr) scattering function.

The assumption of an isotropic scattering function is motivated by the broad scattering characteristics reported by *Saito et al.* [2008, 2010]. The real scattering function for H^+ from the lunar surface has not yet
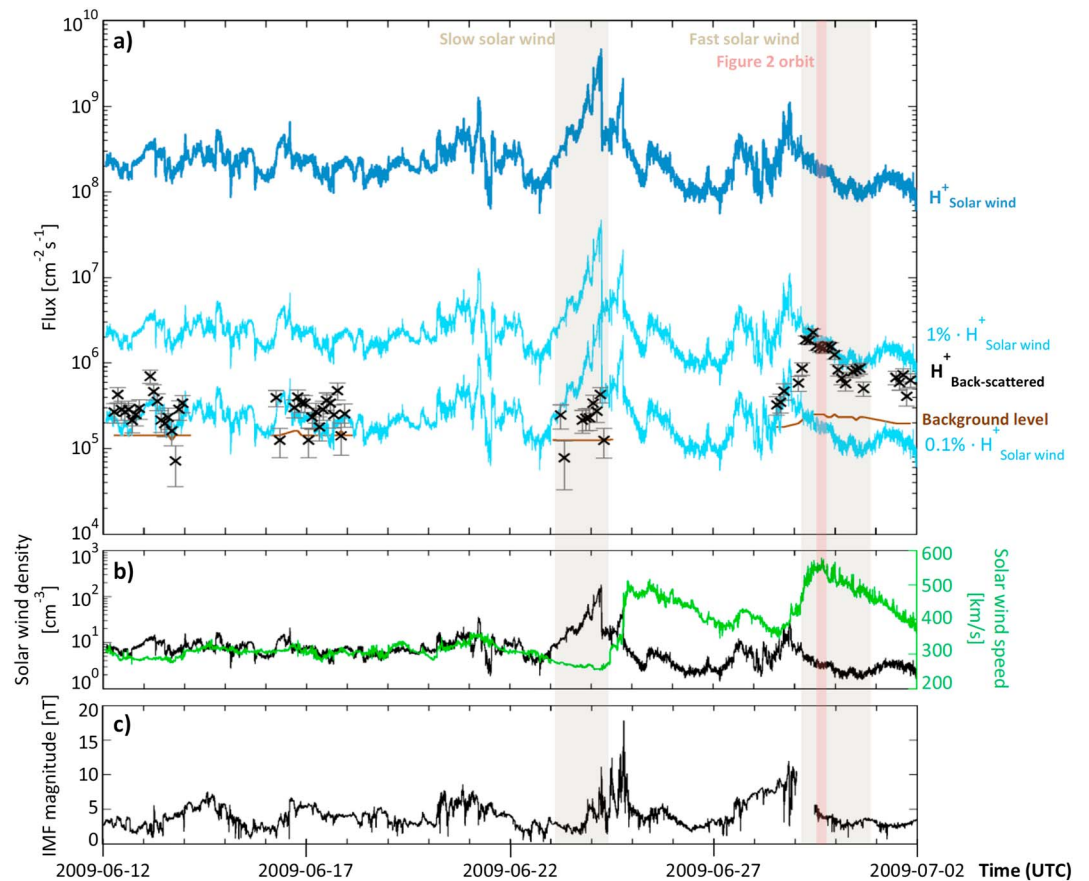
Figure 3. Observations over the interval 12 June to 2 July 2009. (a) The flux of backscattered protons ($H^+_{Backscattered}$, crosses) from the SWIM data and the solar wind flux ($H^+_{Solar\ wind}$, thick line) from Wind/Solar Wind Experiment (SWE). The thin lines represent fractions of 1% and 0.1% of $H^+_{Solar\ wind}$. The expected contribution from the instrument background to the backscattered protons signal is shown as the "Background level." (b) The density and speed of the solar wind measured using Wind/SWE. (c) The interplanetary magnetic field measured using Wind/SWE. Whereas the SWIM data are 20 min averages for each dayside equator crossing, the Wind/SWE data are shifted to account for the solar wind's travel time. The intervals with lowest and highest solar wind speeds are indicated by shaded fields, as is the orbit used in Figure 2.

been reported in detail. Thus, our assumption may cause a systematic bias in the absolute values of the calculated flux. However, the lack of the real scattering function does not introduce much bias in the relative values, because the observation geometry (incident and exiting angles) used in this paper does not change much between orbits (see Figure 1). Another possible approach would be to assume that the scattering function is similar to that of H ENA and use the scattering function described by *Schaufelberger et al.* [2011] (which is updated by *Vorburger et al.* [2013]). However, this assumption is also not validated, and thus, it is not necessarily more accurate. Also, the difference between using the isotropic function and the H ENA function is very small (<10%) for the ranges of solar zenith angle, azimuthal scattering angles and polar scattering angles concerned in this study. Therefore, we have chosen the simpler assumption.

5. The Proton-Backscattering Efficiency

The backscattered H^+ flux for each orbit is shown in Figure 3 along with the solar wind parameters. An approximately linear correlation between the solar wind flux and the backscattered flux can be observed temporarily during periods of tens of hours (e.g., 12–14, 16–18, or 23–24 June). These are times when the solar wind speed is roughly constant. The variation of density by 1 order of magnitude and IMF strength by a factor 2–3 on 23–24 June does not seem to affect the linear correlation between backscattered and solar wind flux. However, at periods when the solar wind speed changes (e.g., 28–29 June), the linear flux correlation is broken. Moreover, comparing periods of different solar wind speed, the backscattered flux

varies from ~1% (e.g., 29–31 June) to ~0.1% (e.g., 16–18 June), and sometimes as little as ~0.01% (e.g., 23–24 June) of the solar wind flux, in correlation with the variations in the solar wind speed. The instrument background is not removed from the flux estimates in Figure 2, but its estimated contribution is shown (i.e., the flux that is equivalent of 1.6 counts per energy-direction bin per 20 min). The background was kept at this stage in order to give upper limit values on the weak backscattering at slow solar wind and to show that the dependence on the solar wind speed is clearly visible even before background reduction.

For a more detailed investigation, we then subtracted the estimated background contribution and plotted the backscattering efficiency η versus the solar wind speed v_{sw}, where η is defined as the ratio of the flux of backscattered H$^+$, or J_{bs}, to the flux of incident solar wind H$^+$, which is denoted by J_{sw}: $\eta = J_{bs}/J_{sw}$. A clear correlation can be observed. We express the backscattering as two separate processes:

$$\eta = P_{bs} \cdot P_{+}, \tag{1}$$

where P_{bs} is the probability of backscattering and P_{+} is the probability for a backscattered particle to be positively charged. Note: Equation (1) is actually just stating: $P(\text{backscattering} \cap \text{positive}) = P(\text{backscattering}) \cdot P(\text{positive} \mid \text{backscattering})$, with the probabilities renamed η, P_{bs}, and P_{+}, respectively. These probabilities and their underlying processes are not well defined for rough insulators. Because the backscattered H$^+$ constitutes a small fraction of the total backscattered population, we approximate P_{bs} to be equal to the H ENA backscattering efficiency and refer to two studies of the H ENA component to find $P_{bs}(v_{sw})$:

$$P_{bs}(v_{sw}) = \text{constant} = 0.19|_{300 < vsw < 550} \tag{2}$$

[*Futaana et al.*, 2012] and

$$P_{bs}(v_{sw}) = \frac{1}{2.3 + 3.3 \cdot 10^{-5}(v_{sw}[\text{km/s}])^2}\Bigg|_{300 < vsw < 600} \tag{3}$$

(*Funsten et al.* [2013], adapted from Figure 10). The difference between these models is small in the context of this paper. However, we will give parameter results for both. For $P_{+}(v_{sw})$, no previous experimental results measured at the Moon are presently available. Thus, we consult laboratory/theoretical studies in which the dependency is often expressed in the following form [e.g., *Eckstein*, 1981; *Niehus et al.*, 1993]:

$$P_{+}(v) = \exp\left(\frac{-v_c}{v}\right), \tag{4}$$

where v_c is a characteristic charge-exchange velocity that is specific to each particle-surface combination. Note that v is typically defined as the perpendicular component of the particle exit velocity [e.g., *Eckstein*, 1981], and in the laboratory it is important to separate v from the velocity component that is parallel to the surface because grazing-angle scattering leads to a very different type of interaction on atomically flat laboratory surfaces [e.g., *Winter*, 2000]. For the rough lunar regolith, a wide range of scattering angles will exist. Moreover, the condition of an atomically flat surface for this special behavior is not true for the regolith. Instead, we define v as the total exit speed. We must then relate v to the known quantity v_{sw}. Elastic collisions and electronic stopping cause energy losses as the proton interacts with the surface. For protons of energies on the order of keV, electronic stopping dominates and causes an energy loss that is typically proportional to the impact energy [e.g., *Niehus et al.*, 1993; *Winter*, 2000; *Draxler et al.*, 2005]. With this assumption, we can assign $v = kv_{sw}$. Using (2) and (4) with $v = kv_{sw}$ in (1) and adding a scaling factor a to account for quantitative errors in the estimation of any combination of η, P_{bs}, and P_{+}, we find

$$\eta = a \cdot 0.19 \exp\left(\frac{-v_c}{kv_{sw}}\right). \tag{5}$$

For the fitting procedures below, the observations were weighted with respect to the estimated errors in η, propagated from the measurement errors and background errors, assuming Poisson distributions. Fitting (5) to the observed $\eta(v_{sw})$ values (Figure 4) yields $a = 2.5$ and $v_c/k = 2500$ km/s. Moreover, using (3) instead of (2) yields

$$\eta = \frac{a}{2.3 + 3.3 \cdot 10^{-5}(v_{sw}[\text{km/s}])^2} \exp\left(\frac{-v_c}{kv_{sw}}\right), \tag{6}$$

where $a = 15$ and $v_c/k = 3000$ km/s. Both (5) and (6) fit the observations well for $v_{sw} > 350$ km/s, but the background noise makes conclusions difficult for the behavior at lower velocities. At lower velocities, the
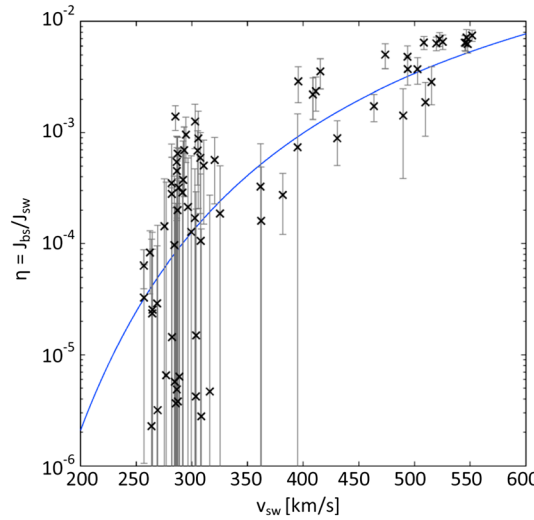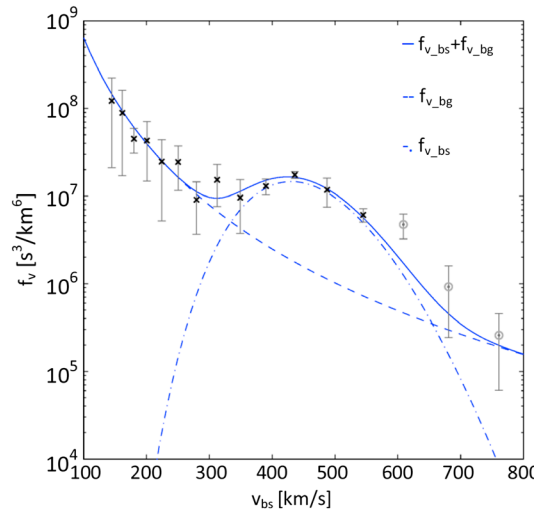
Figure 4. The proton-backscattering efficiency versus the solar wind speed. The crosses indicate the observed ratio between the backscattered flux and the solar wind flux for each dayside equator passing. The estimated instrument background has been subtracted from the observations, and the error bars represent 1σ errors, accounting for Poisson-distributed measurement errors and background errors. The solid line shows the fitted model of equation (5); equation (6) results in a nearly identical curve.

energy loss caused by electronic stopping may be altered by two effects: (1) a minimum required speed for the onset of electronic stopping and (2) a constant energy loss at low impact speeds because of charge exchanges [e.g., *Winter et al.*, 2000; *Draxler et al.*, 2005]. For nongrazing angles and the rough regolith, the latter effect seems more likely (H^+ tends to scatter from the bulk rather than directly at the surface, and it experiences several charge-exchange cycles [e.g., *Eckstein*, 1981; *Souda et al.*, 1995, 1997]).

6. The Speed Distribution Function of Backscattered Protons

We study the speed distribution function of backscattered H^+ for 530 km/s $< v_{sw} < 570$ km/s (Figure 5). We subtract the instrument background and ignore data at $v_{bs} > v_{sw}$, where instrumental crosstalk dominates (section 4). We obtain a mean speed of $\overline{v_{bs}} = 430$ km/s $\approx 0.8 \cdot v_{sw}$, with a spread that can be approximated by a normal distribution with $\sigma_{vbs} = 85$ km/s. Note that these values were obtained at $v_{sw} \approx 550$ km/s. At lower solar wind speeds, the shape of the distribution cannot be well defined. As a test of the reasoning presented in the previous section, we assume that the H^+ speed distribution is the product of the total speed distribution (which is dominated by H ENA) and the probability of backscattering with a positive charge: $f(v_{bs}) = f(v_{bs\_Tot}) \cdot P_+(v_{bs})$. Using $f(v_{bs\_Tot})$ from *Futaana et al.* [2013] with $v_{sw} = 550$ km/s and (4), where $v = v_{bs}$, we obtain the model

$$f(v_{bs}) \propto \exp\left[-m_p(v_{bs})^2/2(550 \cdot 0.273 - 1.99)\right]$$
$$\cdot \exp\left(\frac{-v_c}{v_{bs}}\right), \qquad (7)$$

which fits the observations (Figure 5) and has the fitted parameter $v_c = 5000$ km/s. Using $k = \overline{v_{bs}}/\overline{v_{sw}} = 0.8$, this gives a $v_c/k \approx 6000$ km/s, a factor 2 larger than that suggested by the previous section.

7. Discussion and Conclusions

Using SARA:SWIM on Chandrayaan-1, we observed H^+ scattered from the lunar surface, which exhibited characteristics (Figure 2) consistent with the previous observations by Kaguya [*Saito et al.*, 2008]. We found that the H^+ backscattering efficiency strongly depends on the solar wind velocity: ~1% of the solar wind backscattered as H^+ for $v_{sw} \approx 550$ km/s, whereas ~0.01% backscattered as H^+ for $v_{sw} \approx 250$ km/s (Figures 3 and 4). The weakest observations of backscattered fluxes in Figure 3 are comparable to the instrument background levels, so the backscattering efficiency at low solar wind speeds may be even lower (see Figure 4, where the background has been subtracted).

Figure 5. The velocity distribution function of backscattered protons for solar wind speeds of 525–575 km/s. The symbols (namely, the crosses up to the solar wind velocity and circles above it) represent the average observed distribution function, which has been normalized to a solar wind flux of 2×10^8 cm^{-2} s^{-1}. The solid line represents the sum of a velocity distribution (f_{v_bs}), which is given by equation (7), and the fitted instrument background (corresponding to 1.6 counts per energy-direction bin per 20 min) (f_{v_bg}). The error bars represent 1σ Poisson errors of the observations.

After formulating the H^+ backscattering efficiency as the product of the total (H ENA-dominated) backscattering efficiency and the probability of a positively charged state after a collision, we used previous H ENA observations and laboratory/theoretical studies to formulate different models (equations (5) and (6)) that we fitted to the observed speed dependence. The models assumed an energy loss at the surface proportional to the impact energy and reproduced the observations well above $v_{sw} = 350$ km/s. At lower speeds, it is possible that the dependence changes, e.g., due to a constant additional energy loss from charge-exchange cycles. However, the uncertain measurements at low speeds do not allow conclusions on this issue. Additionally, the H ENA models that we used (2) and (3) have not been verified for $v_{sw} < 300$ km/s (although our ENA observations for this period, not shown, revealed no obvious deviation from the characteristics reported by *Futaana et al.* [2012]). Therefore, further studies are required to determine whether the dominant energy loss mechanism changes at lower impact velocities.

A few orbits corresponding to the slowest solar wind also involve a large increase in the solar wind density. Comparing the peak with adjacent points with lower density reveals no significant density dependence. Also, it seems unlikely from a theoretical point of view that there would be any collective effects that would change the particle-surface interaction by a temporarily increased impact rate (~10^{-5} s^{-1} for each surface atom).

We also examined the speed distribution of the backscattered H^+ (Figure 5), which had a peak at ~80% of the solar wind speed, and a spread σ_{vbs} of 85 km/s, for $v_{sw} \approx 550$ km/s. Similar to the case of the backscattering efficiency, the H^+ speed distribution can be qualitatively explained using the product of the H ENA speed distribution and the probability of a positively charged state (equation (7)). The different approaches gave different estimates of the characteristic charge-exchange velocity v_c by a factor of 2 (equations (5) and (6) versus (7)), which is not unreasonable considering the approximations and uncertainties involved in the analysis.

The observed peak of the backscattered H^+ at 0.8 v_{sw} corresponds to an energy loss of approximately 40%. Assuming that the average mass of the surface atoms is approximately 20 amu [*Wurz et al.*, 2007], the mass ratio between the target and the impinging particle is $A = 20$. The relative energy loss in a single binary collision is given by $2/A < \Delta E/E < 4/A$ [*Niehus et al.*, 1993], which suggests that the backscattered H^+ ions (in the case of $v_{sw} \approx 550$ km/s) have experienced two to three collisions on average.

In addition to providing some insights into the interaction physics, the results further elucidate the complexity of the lunar environment. H^+ reflected from LMAs (which decreases with increasing solar wind dynamic pressure [*Vorburger et al.*, 2012]) and H^+ reflected from the regolith have opposite dependencies on the solar wind velocity, which allows the interaction between the solar wind and the Moon to shift from an anomaly dominated to a surface-dominated interaction and vice versa. These findings can also provide context for plasma observations at other objects. For example, at the Martian moon Phobos, *Futaana et al.* [2010a] reported a H^+ backscattering efficiency of ~0.5%–10% from a single flyby observation. The solar wind velocity at the time of the Phobos observations was high (520 km/s). Thus, the corresponding backscattering efficiencies derived for the Moon would be ~1%, which is within the uncertainty reported at Phobos.

The empirical formulae obtained here can be useful for investigations of other characteristics of backscattered H^+, such as the scattering function, for which normalization with respect to the velocity dependence may be required. These formulae may also be applicable for remote sensing. From an observed backscattering efficiency, the particle impact velocity can be deduced, which can then be compared with the upstream velocity to calculate the surface potential (see *Futaana et al.* [2013] for a similar study using H ENA). Observations in the present study took place at the lunar far side and thus mainly at highland regions. Future comparison with mare regions may provide clues to the scattering as a function of surface structure and composition. Eventually, the principles of low-energy ion scattering spectrometry [e.g., *Niehus et al.*, 1993] may be applied to the remote sensing of the surface composition and/or surface structure of airless bodies in space using the solar wind or some other naturally occurring plasma as the incident beam.

References

Allegrini, F., et al. (2013), Lunar energetic atom (ENA) spectra measured by the interstellar boundary explorer (IBEX), *Planet. Space Sci.*, *85*, 232–242, doi:10.1016/j.pss.2013.06.014.

Bandurko, V. V., N. N. Koborov, V. A. Kurnaev, V. M. Sotnikov, and O. V. Zabeyda (1990), Low energy hydrogen and helium backscattering from surfaces with structure, *J. Nucl. Mater.*, *176–177*, 630–634, doi:10.1016/0022-3115(90)90118-7.

Barabash, S., et al. (2009), Investigation of the solar wind-Moon interaction onboard Chandrayaan-1 mission with the SARA experiment, *Curr. Sci.*, *96*(4), 526–532.

Draxler, M., S. P. Chenakin, S. N. Markin, and P. Bauer (2005), Apparent velocity threshold in the electronic stopping of slow hydrogen ions in LiF, *Phys. Res. Lett.*, *95*, 113201, doi:10.1103/PhysRevLett.95.113201.

Eckstein, W. (1981), Charge fractions of reflected particles, in *Inelastic Particle-Surface Collisions*, pp. 157–183 , Springer, Berlin Heidelberg.

Funsten, H. O., et al. (2013), Reflection of solar wind hydrogen from the lunar surface, *J. Geophys. Res. Planets*, *118*, 292–305, doi:10.1002/jgre.20055.

Futaana, Y., S. Barabash, M. Holmström, A. Fedorov, H. Nilsson, R. Lundin, E. Dubinin, and M. Fränz (2010a), Backscattered solar wind protons by Phobos, *J. Geophys. Res.*, *115*, A10213, doi:10.1029/2010JA015486.

Futaana, Y., S. Barabash, M. Wieser, M. Holmström, A. Bhardwaj, M. B. Dhanya, R. Sridharan, P. Wurz, A. Schaufelberger, and K. Asamura (2010b), Protons in the near-lunar wake observed by the Sub-keV Atom Reflection Analyzer on board Chandrayaan-1, *J. Geophys. Res.*, *115*, A10248, doi:10.1029/2010JA015264.

Futaana, Y., S. Barabash, M. Wieser, M. Holmström, C. Lue, P. Wurz, A. Schaufelberger, A. Bhardwaj, M. B. Dhanya, and K. Asamura (2012), Empirical energy spectra of neutralized solar wind protons from the lunar regolith, *J. Geophys. Res.*, *117*, E05005, doi:10.1029/2011JE004019.

Futaana, Y., S. Barabash, M. Wieser, C. Lue, P. Wurz, A. Vorburger, A. Bhardwaj, and K. Asamura (2013), Remote energetic neutral atom imaging of electric potential over a lunar magnetic anomaly, *Geophys. Res. Lett.*, *40*, 262–266, doi:10.1002/grl.50135.

Halekas, J. S., Y. Saito, G. T. Delory, and W. M. Farrell (2011), New views of the lunar plasma environment, *Planet. Space Sci.*, *59*(14), 1681–1694, doi:10.1016/j.pss.2010.08.011.

Lue, C., Y. Futaana, S. Barabash, M. Wieser, M. Holmström, A. Bhardwaj, M. B. Dhanya, and P. Wurz (2011), Strong influence of lunar crustal fields on the solar wind flow, *Geophys. Res. Lett.*, *38*, L03202, doi:10.1029/2010GL046215.

McCann, D., S. Barabash, H. Nilsson, and A. Bhardwaj (2007), Miniature ion mass analyser, *Planet. Space Sci.*, *55*, 1190–1196, doi:10.1016/j.pss.2006.11.020.

McComas, D. J., et al. (2009), Lunar backscatter and neutralization of the solar wind: First observations of neutral atoms from the Moon, *Geophys. Res. Lett.*, *36*, L12104, doi:10.1029/2009GL038794.

Niehus, H., W. Heiland, and E. Taglauer (1993), Low-energy ion scattering at surfaces, *Surf. Sci. Rep.*, *17*(4–5), 213–303, doi:10.1016/0167-5729(93)90024-J.

Purucker, M. E., and J. B. Nicholas (2010), Global spherical harmonic models of the internal magnetic field of the Moon based on sequential and coestimation approaches, *J. Geophys. Res.*, *115*, E12007, doi:10.1029/2010JE003650.

Rodríguez, M. D. F., L. Saul, P. Wurz, S. A. Fuselier, H. O. Funsten, D. J. McComas, and E. Möbius (2012), IBEX-Lo observations of energetic neutral hydrogen atoms originating from the lunar surface, *Planet. Space Sci.*, *60*(1), 297–303, doi:10.1016/j.pss.2011.09.009.

Saito, Y., et al. (2008), Solar wind proton reflection at the lunar surface: Low energy ion measurement by MAP-PACE onboard SELENE (KAGUYA), *Geophys. Res. Lett.*, *35*, L24205, doi:10.1029/2008GL036077.

Saito, Y., et al. (2010), In-flight performance and initial results of Plasma Energy Angle and Composition Experiment (PACE) on SELENE (Kaguya), *Space Sci. Rev.*, *154*(1-4), 265–303, doi:10.1007/s11214-010-9647-x.

Schaufelberger, A., P. Wurz, S. Barabash, M. Wieser, Y. Futaana, M. Holmström, A. Bhardwaj, M. B. Dhanya, R. Sridharan, and K. Asamura (2011), Scattering function for energetic neutral hydrogen atoms off the lunar surface, *Geophys. Res. Lett.*, *38*, L22202, doi:10.1029/2011GL049362.

Souda, R., K. Yamamoto, W. Hayami, T. Aizawa, and Y. Ishizawa (1995), Low-energy H^+, He^+, N^+, O^+, and Ne^+ scattering from metal and ionic-compound surfaces: Neutralization and electronic excitation, *Phys. Rev. B*, *51*(7), 4463–4474, doi:10.1103/PhysRevB.51.4463.

Souda, R., T. Suzuki, and K. Yamamoto (1997), Neutralization and electronic excitation during low-energy H and He scattering from LiF, *Surf. Sci.*, *397*, 1–3, doi:10.1016/S0039-6028(97)00719-X.

Vorburger, A., P. Wurz, S. Barabash, M. Wieser, Y. Futaana, M. Holmström, A. Bhardwaj, and K. Asamura (2012), Energetic neutral atom observations of magnetic anomalies on the lunar surface, *J. Geophys. Res.*, *117*, A07208, doi:10.1029/2012JA017553.

Vorburger, A., P. Wurz, S. Barabash, M. Wieser, Y. Futaana, C. Lue, M. Holmström, A. Bhardwaj, M. B. Dhanya, and K. Asamura (2013), Energetic neutral atom imaging of the lunar surface, *J. Geophys. Res. Space Physics*, *118*, 3937–3945, doi:10.1002/jgra.50337.

Wieser, M., S. Barabash, Y. Futaana, M. Holmström, A. Bhardwaj, R. Sridharan, M. B. Dhanya, P. Wurz, A. Schaufelberger, and K. Asamura (2009), Extremely high reflection of solar wind protons as neutral hydrogen atoms from regolith in space, *Planet. Space Sci.*, *57*(14–15), 2132–2134, doi:10.1016/j.pss.2009.09.012.

Winter, H. (2000), Scattering of atoms and ions from insulator surfaces, *Prog. Surf. Sci.*, *63*, 117–247, doi:10.1016/S0079-6816(99)000020-9.

Wurz, P., U. Rohner, J. A. Whitby, C. Kolb, H. Lammer, P. Dobnikar, and J. A. Martín-Fernández (2007), The lunar exosphere: The sputtering contribution, *Icarus*, *191*, 486–496, doi:10.1016/j.icarus.2007.04.034.